Surface & Coatings Technology 374 (2019) 822–832

Contents lists available at ScienceDirect

Surface & Coatings Technology

journal homepage: www.elsevier.com/locate/surfcoat

Tunable microstructures and morphology of zirconium films via an assist of magnetic field in HiPIMS for improved mechanical properties

Huan Luo[a,*], Fei Gao[b], Alain Billard[a]

[a] FEMTO-ST, UMR 6174 CNRS, MN2S, Univ. Bourgogne Franche-Comté, UTBM, Site de Montbéliard, 90000 Belfort Cedex, France
[b] FEMTO-ST, UMR 6174 CNRS, Energy Department, Univ. Bourgogne Franche-Comté, UTBM, Rue Thierry Mieg, 90000 Belfort Cedex, France

ARTICLE INFO

Keywords:
HiPIMS
Magnetic field configuration
Zirconium film
OES
Hardness

ABSTRACT

Although HiPIMS technology has been widely studied, its optimization still remains in the adjustment of the experimental parameters acting on the ions, such as impulse mode, due to the inherent complexity of partially magnetized plasma of HiPIMS. Herein, recapture and re-energy of electrons by the assistance of the A-type magnetic field configuration, constructed by field coupling of the cathode magnetron and the auxiliary magnets mounted behind the substrate holder, was proposed. The dynamic behavior of the ions is attempted to be guided by exploiting electron recapture. The studies on the plasma diagnosis by optical emission spectroscopy and magnetic field simulation revealed that when the cathodic discharge remains constant, the characteristics of the deposition plasma in front of the substrate can be altered. Zirconium films were prepared under the a-HiPIMS mode (operated with the A-type magnetic configuration) and the conventional HiPIMS mode. Results showed that the Zr films prepared in the a-HiPIMS mode exhibited smoother surface, denser morphology, finer grains, higher homogenous thickness distribution, higher hardness, enhanced elastic recovery and higher value of the ratios H/E^* and H^3/E^{*2}. The mechanism of microstructure evolution of Zr film was discussed. It demonstrated that the action of the A-type magnetic configuration can densify the Zr film, without the need for high energy ion bombardment. The A-type magnetic field configuration provided an alternative strategy for compensating for the shortcoming of substrate bias in HiPIMS, invalidity to electrical insulating substrates, in terms of the dense film.

1. Introduction

The transition metal zirconium with hexagonal close-packed crystal structure has excellent properties, such as low neutron absorption cross section, relatively high melting temperature (1855 °C), good mechanical properties and excellent resistance to corrosive attack in most salts, organic and inorganic acid solutions [1–3]. Therefore, zirconium is recognized in many industrial applications. In nuclear reactors and spaceflight applications, zirconium has been broadly used owing to its low neutron absorption cross section, high melting temperature and mechanical properties [4–7]. The physical properties (high thermal conductivity, minimum creep property and strength) and chemical properties of zirconium in harsh working environments (high temperature and high pressure) promote its use in the manufacture of molten metal crucibles, gas turbines, rocket engine tubes and ultra-high frequency furnaces [8]. A. Singh et al. [9] investigated the effect of substrate temperature on the growth characteristics of zirconium films in the pulsed magnetron sputtering. J. Chakraborty et al. [10] studied the relationship between stress, texture and film thickness in Zr films prepared by DC magnetron sputtering. Literatures [11,12] provided additional information on the conditions required for the formation of ω-phase in the zirconium film, with a focus on the effects of the substrate, inter-layers and bias voltage.

High power impulse magnetron sputtering (HiPIMS) characterized by the high peak power is a well-established ionized physical vapor deposition (IPVD) technique. In HiPIMS discharge, the high power is delivered via unipolar pulses with low repetition frequency and low duty cycle [13]. Such a power supply mode results in a high-density plasma above the cathode target. It allows the preparation of films with superior properties [14], especially compared to DC magnetron sputtering. Moreover, this power mode facilitates adjustment of plasma characteristics that primarily affect film growth, such as through discharge current, voltage, pulse frequency and duration. Therefore, the HiPIMS technique plays a pivotal role in controlling thin film growth and tailoring the film properties to meet the needs of specific applications.

* Corresponding author.
E-mail address: huan.luo@utbm.fr (H. Luo).

https://doi.org/10.1016/j.surfcoat.2019.06.072
Received 4 March 2019; Received in revised form 28 May 2019; Accepted 24 June 2019
Available online 26 June 2019

In order to prepare higher quality films with advanced properties and expand the application range of HiPIMS, the control of the HiPIMS discharge process has been extensively studied. The approaches of adjusting the experimental parameters, such as substrate bias [14], substrate temperature [9,15], impulse repetition frequency [16] and working pressure [17], has been adopted in the past few years. Among them, the application of the substrate bias is very effective in improving the mechanical properties of the thin film, since the HiPIMS plasma characterized by a high ionization rate can be effectively affected by the electric field induced by the bias. However, the application of substrate bias does not contribute to electrically insulating substrates, such as oxidizing material and polymer, which are widely applied in the industry from packaging or optics to medicine [18–20]. This unavailability of substrate bias greatly limits the range of applications of HiPIMS. Moreover, almost all approaches that have been used are aimed directly at ions in the plasma, such as using a substrate bias to accelerate ion motion, adjusting the pulse mode to weaken the back attraction of ions, and changing the working pressure to adjust the ionization rate. It seems to be because these approaches are relatively easy to control and implement. Due to the inherent complexity and microscopic instability of the partially magnetized plasma in the HiPIMS discharge [21], at present, there is hardly any literature that has optimized the discharge process of HiPIMS through the most important magnetized electron.

In addition to the optimization approaches that are still limited to controlling experimental parameters, the effects of different magnetic field configurations on film growth have also been reported [22–25]. External magnets [22] or coils [23] placed above the magnetron for increasing the deposition rate and improving the film quality have been investigated. However, these arrangements of magnets or coils further introduce complexity into the vacuum system. The direct contact of the magnets and coils with the plasma may interfere with the plasma kinetics above the target and thus disrupt the stability of the plasma discharge. Other forms of magnetic field configurations for controlling plasma behavior and film microstructure have not been designed and proposed yet. Moreover, few studies have focused on changing the behavior of plasma in front of the substrate, which is a more precise “control button” (for changing the film properties) than plasma in the magnetron cathode. For the plasma in cathode trap, they will encounter some unknown and unpredictable variations during motion toward the substrate.

The present work aimed to control the electron dynamic near the substrate in an attempt to guide the behavior of the ions during HiPIMS discharge, and thus to adjust the characteristics of the plasma near the substrate. In order to achieve this indirect control from electrons link to ions, an A-type magnetic field configuration was proposed. This magnetic field configuration was simulated by the finite element method. The plasma characteristics near the substrate under the A-type magnetic field were diagnosed by optical emission spectroscopy (OES). The mechanism of changes in plasma characteristics was discussed. Moreover, the Zr films were prepared in the conventional HiPIMS mode and in the a-HiPIMS mode (operated in the A-type magnetic configuration), respectively. The microstructure and mechanical properties of Zr films were characterized and finally discussed. It should be emphasized that the conventional HiPIMS mode was used as a benchmark for comparison rather than DC magnetron sputtering. It is known that HiPIMS-prepared films are superior to DC-prepared films in terms of mechanical properties. Therefore, although the comparison result looks fantastic in the DC benchmark, it does not contribute substantially to highlighting the advantages of the a-HiPIMS approach in achieving high-quality films.

2. Experimental details

2.1. A-type magnetic field configuration

In the HiPIMS plasma, the Larmor radius of electrons is much smaller than the characteristic dimension of the HiPIMS system. The electrons are magnetized and therefore controlled by the interaction of the electric field and the magnetic field. Since the electrons have very high velocities (powered by electric and magnetic fields), their perturbation potential can easily act on ion behavior even if their mass is small [26]. Meanwhile, the ions are unmagnetized and only controlled by the equilibrium and perturbation electric potential [27]. Based on this scenario, the energy of the sputtered ion flux that contributes to the film growth originates from two sources. The first source is the kinetic energy carried by the ions themselves. This energy is provided by the initial bombardment of argon ions, a portion of which is lost due to collision with the gas phase on the path from the target to the substrate. The second source is provided by the net Coulomb force exerted by the electrons moving across the magnetic field lines toward the substrate [28,29]. Here, we look at the latter. The focus is on controlling the trajectory of the electrons, which in turn directs the ion behavior by net Coulomb force.

In order to achieve this goal, the A-type magnetic field configuration is designed by superimposing an auxiliary magnetic field on the field of the cathode magnetron. The auxiliary magnetic field is supported by a circularly arranged permanent magnets placed behind the substrate holder, the schematic diagram of which is depicted in Fig. 1. The polarity of the auxiliary magnetic field facing the target is opposite to the magnetic pole of the magnetron outer ring. For purpose of the deeper investigation of the A-type magnetic field configuration effect on the film growth, three different strength of auxiliary magnetic fields were performed, which were recorded as B_1, B_2, and B_3, respectively. The HiPIMS discharges operating in the different auxiliary magnetic fields are referred to as the a-HiPIMS ($\_B_1/\_B_2/\_B_3$), and the conventional HIPIMS without auxiliary magnetic field is abbreviated as the c-HiPIMS.

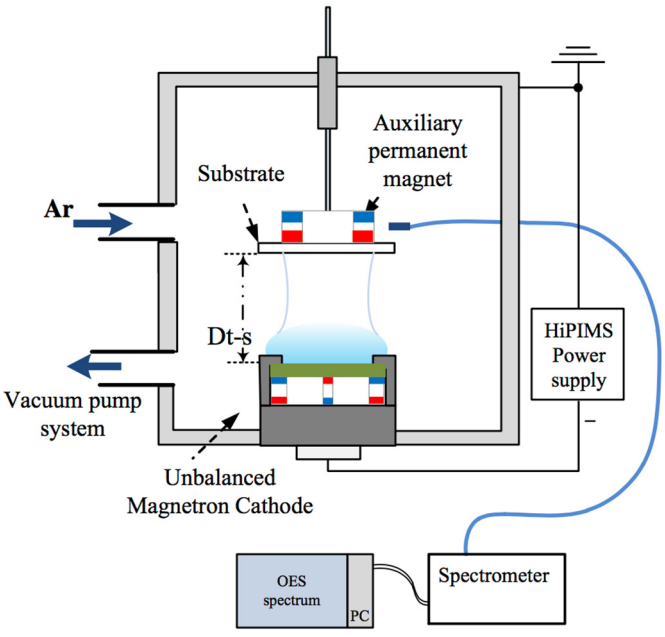

Fig. 1. Simplified schematic of the HiPIMS system with the A-type magnetic field configuration.

2.2. Deposition of Zr films

All the deposition samples of Zr films were carried out on glass and stainless steel substrates, by sputtering the pure Zr metallic target (150 mm in diameter and 8 mm thick, 99.5% purity). In the vacuum chamber, the substrate holder was floated and the unbalanced magnetron was powered by HiPIMS (Hüttinger Elektronik) operating in the unipolar mode. The distance between the substrate holder and the target $D_{t\text{-}s}$ was 10 cm. For substrate, no intentional heating was applied and no discharge voltage bias (DC bias) was employed. Prior to all deposition, the vacuum chamber was evacuated using a turbomolecular pump to a base pressure of $< 1 \times 10^{-3}$ Pa. During depositions, argon was used as the working gas. Its mass flow rate was kept constant at 200 standard cubic centimeter per minute (sccm), and the working pressure was maintained at 0.4 Pa. For the deposition modes, the target discharge voltage was set as −600 V and the average discharge current was maintained at 1 A. The impulse repetition frequency was 500 Hz, while the impulse duration was set as 42 μs in the c-HiPIMS mode. In the cases of a-HiPIMS modes, the pulse duration was adjusted to keep the cathode discharge parameters constant (current and voltage) under the different strength of auxiliary magnetic fields. In order to avoid the effect of thickness on the microstructure and properties of the Zr films, the preparation time was adjusted to keep the thickness of all films to be at 1.5 μm consistently. The specific values of the deposition parameters are shown in Table 1.

2.3. Characterizations of plasma and films

The magnetic field configurations of c-HiPIMS and three a-HIPIMS modes were simulated by using the finite element method. Since the plasma parameter is the key factor in controlling the growth of the film, the plasma near the substrate space was diagnosed by optical emission spectroscopy (OES) measurements using the Acton Research Corporation Spectra Pro-500i. The entrance of the optical fiber was placed in the chamber in such a way that the light emission signals of the region below substrate can be collected. The plasma emission signals were recorded in the spectral range of 285–800 nm.

The film thickness was determined by the step method with the Altysurf profilometer produced by Altimet, equipped with the inductive probe. Before each measurement, the device was calibrated by the reference sample numbered 787569 which is accredited by the CETIM organization. In order to examine the structural characteristics of Zr films, the Bragg Brentano configuration X-ray diffraction (BRUKER D8) with the Co (λ = 1.78897 Å) source at a current of 40 mA and a voltage of 35 kV was used. Diffractograms were collected under air flow in the 20–80° angle range at a scan rate (2θ) of $0.1^{\circ}\,s^{-1}$. Film morphology was observed on the top surface and brittle fracture cross section by using the JEOL JSM-7800F field emission gun scanning electron microscope (FEG-SEM).

The nanohardness and effective Young's modulus of the films were carried out by using the Nanoindentation Tester (applied load is 5 mN) from CSM Instruments, equipped with a Berkovich diamond indenter tip at room temperature. The nanoindentation data were the average of twelve measurements performed for each sample and determined based on the Oliver-Pharr model [30]. In order to eliminate the substrate effect, the indentation depth was kept < 10% of the film thickness during measurement. The radius of curvature (R) of the as-deposited film was measured by the Altysurf profilometer equipped with the optical probe. The residual stress inside the film was calculated according to the Stoney formula [31]:

$$\sigma = \frac{E_s}{6(1-\upsilon_s)}\frac{d_s^2}{d_f}\frac{1}{R} \quad (1)$$

in which E_s, d_s and υ_s represent Young's modulus, thickness and Poisson's ratio of the substrate, respectively. d_f stands for the thickness of the film. The toughness of the film was examined by the Vickers indenter (Leica, VMHT30A) with a load of 20 N for 15 s. After testing, the indentation morphologies were examined in the JEOL JSM-7800F FEG-SEM.

Table 1
Specific preparation parameters corresponding to the different deposition modes.

Batch no.	Auxiliary **B** (mT)	Deposition time (min)	Pulse width (μs)
1	c-HiPIMS	48	42
2	a-HiPIMS_B_1 (15 mT)	60	38
3	a-HiPIMS_B_2 (30 mT)	83	34
4	a-HiPIMS_B_3 (45 mT)	100	30

3. Results and discussion

3.1. Magnetic field configuration and plasma characteristics

Numerous experiments have shown that the microstructure of the film is affected by the ion energy distribution and the fraction of ionized species in the deposition plasma [16,17,22]. These plasma characteristics, in turn, are closely related to the magnetic field distribution in the vacuum chamber. Therefore, the magnetic field simulation of the c-HiPIMS and a-HiPIMS modes and the plasma diagnosis of the corresponding modes were carried out. Moreover, combined with the magnetic field simulation, the change of the plasma motion behavior and its driving mechanism under the A-type magnetic field configuration were analyzed.

3.1.1. Simulation of the magnetic field configuration

The magnetic field configurations for c-HiPIMS and three a-HiPIMS_B_1/B_2/B_3 modes were simulated by using the finite element method. The dimension of the magnetron and the auxiliary permanent magnets in the simulation is the same as that in the actual deposition chamber. Fig. 2 shows the simulation results of c-HiPIMS and a-HiPIMS_B_3 which has the strongest magnetic strength in the three a-HiPIMS modes.

In the magnetic field distribution of Fig. 2, the magnetic strength is marked by a different color, and the magnetic line is depicted by the solid black line. In order to clearly describe the difference in the magnetic field configuration between the a-HiPIMS mode and the c-HiPIMS mode, the space between the magnetron and the substrate is separated to three regions, as indicated by the white dotted line in Fig. 2(b). Due to the use of an unbalanced magnetron, the magnetic field distribution of the c-HiPIMS mode, Fig. 2(a), exhibits a type II unbalanced magnetic trap. A portion of the magnetic field lines diverges from the magnetron to the vacuum chamber wall. Obviously, in Fig. 2(b), the auxiliary magnets have a significant coupling effect with the magnetron. The magnetic field distribution between the substrate and the magnetron shows distinct differences.

In front of the substrate, a part of the magnetic lines of the auxiliary magnetic field attracts and connects to the outer pole of the magnetron. Another part of the magnetic lines forms a closed loop in front of the substrate. This results in two changes in the magnetic field in the region I and region II. In region I, a new magnetic trap is formed. Due to the self-biasing effect of the substrate in the HiPIMS discharge, the space of the new magnetic trap produces a sub-E × B region. Its structure (orthogonal electric and magnetic fields) is exactly the same as the ionization region above the cathode magnetron, in which the magnetic and electric field strength are relatively weak. In region II, due to the attraction of the outer pole of the magnetron, the magnetic lines are guided to converge toward the substrate to a greater extent. Whereas in the c-HiPIMS mode, they diverge toward the reactor wall. The racetrack region is defined by the area above target where the electric field and magnetic field are strictly orthogonal. It largely dominates the

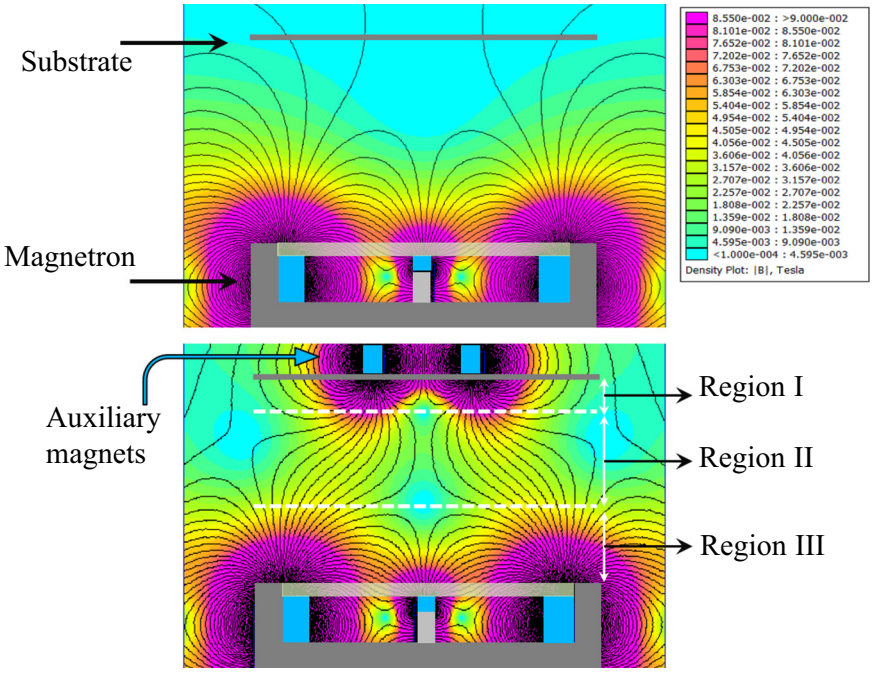

Fig. 2. Magnetic field simulations of (a) c-HiPIMS mode and (b) a-HiPIMS_B_3 mode.

utilization of the target. In region III, it can be seen that the racetrack region is slightly widened toward the target edge in the a-HiPIMS_B_3 mode. It exhibits a conical and narrow distribution (pattern of magnetic lines) in the c-HiPIMS mode.

According to the magnetic field distributions, when the A-type magnetic field is applied, (i) the sub-E × B region is formed and (ii) more magnetic lines are focused toward the substrate. (iii) The parallel magnetic field distribution above magnetron cathode is broadened. These three features predict that the plasma dynamics near the substrate can be adjusted when the discharge conditions close to the target remain constant. In order to quantitatively estimate the effect of the A-type magnetic field on the plasma parameters, the plasma composition at the sub-E × B region is characterized by using optical emission spectroscopy (OES).

3.1.2. Plasma characteristics from OES

The plasma characteristics performed by OES during the discharge process are shown in Fig. 3. In order to make the spectra clearly distinguishable, the results of a-HiPIMS_B_1 and a-HiPIMS_B_2 are not given simultaneously. The orange spectrum corresponds to the plasma in the c-HiPIMS mode, and the blue spectrum corresponds to the plasma in the a-HiPIMS_B_3 mode. It is obvious that the application of the A-type magnetic field leads to quite different plasma characteristics. The intensities of the emission lines originated from the ionized Zr^+ and Ar^+ species are significantly increased, and the increment of Ar^+ seems to be stronger than that of Zr^+, indicated in Fig. 3(a). The intensities of emission lines at the excited neutrals Zr^0 and Ar^0 are approximately the same.

Here, a detailed analysis is necessary to clarify the interesting diagnostic difference in Fig. 3(a). The emission intensity ratio of I^M/I^{Ar^0} (where I^M represents the intensity of Ar^+, Zr^+ and Zr^0 lines, and I^{Ar^0} represents the intensity of Ar^0 line) are shown in Fig. 4. The orange bars represent all ratio values in the c-HiPIMS mode, and the blue bars represent all ratio values in the a-HiPIMS_B_3 mode. In the calculation of the emission intensity ratio I^M/I^{Ar^0}, for each species, three specific emission lines with comparable energy levels were used. In the ratio I^{Ar^+}/I^{Ar^0} (left column), three patterns (including cross grid, horizontal stripe, and vertical stripe) represent three emission lines at 442.6 nm, 480.6 nm and 487.9 nm of Ar^+ respectively. In the ratio I^{Zr^+}/I^{Ar^0} (middle column), three patterns represent three emission lines at 339.2 nm, 343.8 nm and 349.6 nm of Zr^+ respectively. Similarly, three patterns represent 360.1 nm, 386.4 nm and 389.1 nm emission lines of Zr^0 in the ratio I^{Zr^0}/I^{Ar^0} (right column). For the denominator of each ratio Ar^0, the average value of the emission intensities of 750.4 nm, 763.5 nm and 794.8 nm was chosen. It should be noted that the emission lines at the position of 434.8 nm were not used in the calculation, whether for Zr^0 or Ar^+, since they almost overlap, as shown in Fig. 3(b).

The evolution of the ratio of I^{Ar^+}/I^{Ar^0} and I^{Zr^+}/I^{Ar^0} indicates an increase in the ionization rate of the working gas and the target species in front of the substrate in the a-HiPIMS_B_3 mode. The emission intensity of Ar^+ increased by an average of 3 times, while that of Zr^+ increased by an average of 0.5 times. It may be interpreted as a consequence of the formation of the sub-E × B region and the convergence of the magnetic lines toward the substrate.

In addition to the OES results, the enhanced plasma density in front of the substrate is also confirmed by the visual inspection during plasma discharge and the pulse duration (that varied to maintain a constant cathode discharge). In the a-HiPIMS modes, a small and brighter plasma region can be seen with a size of about 2.5 cm extending below the substrate position. While the cathode discharge current and voltage are kept constant, the reduced pulse duration is required in the a-HiPIMS modes. As the strength of the auxiliary magnetic field increased from 0 to 45 mT, the pulse duration was decreased from 42 to 30 μs, depicted in Table 1.

3.1.3. Discussion on changes in plasma characteristics

From OES diagnostic results, it is suggested that the A-type magnetic field in the a-HiPIMS mode allows the high-density plasma to be no longer strictly limited in the magnetic trap. The plasma is guided toward the substrate, the collision and ionization rate in the vicinity of the substrate are enhanced. The reason for the former variation (plasma is guided) is that the magnetic lines act as the focusing lens for the ionized deposition material, which has been reported in [23,32]. However, the mechanism has not been explained clearly because the ions are unmagnetized. The latter variation (enhanced collision and ionization rate) is caused by the recapture and re-energy of the electrons in the sub-E × B region, which is first proposed in the present work. Here, the mechanisms of these two variations are explained in

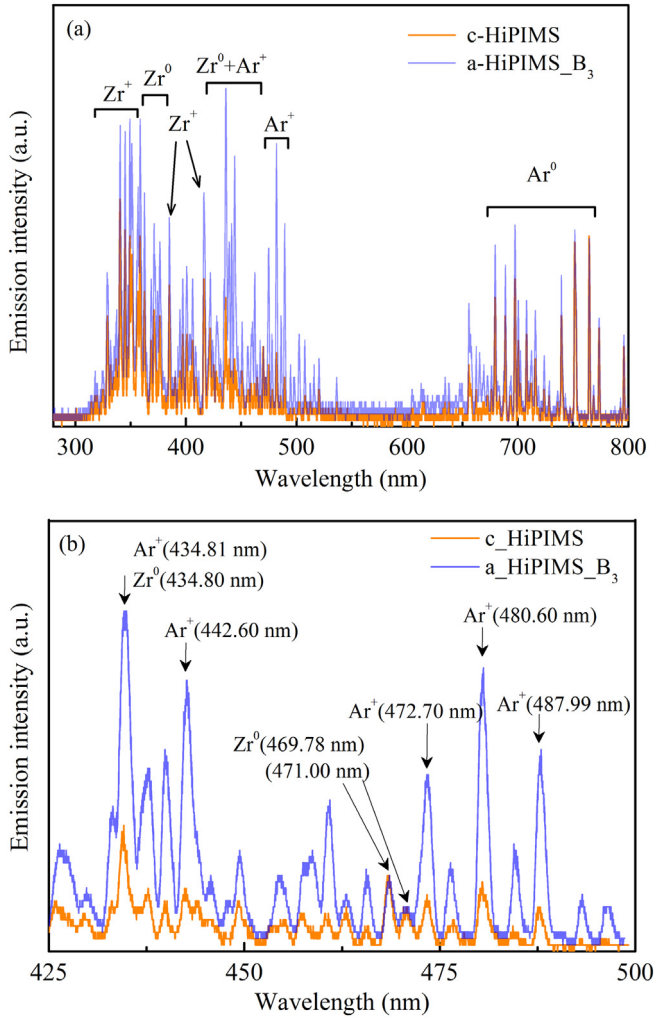

Fig. 3. Optical emission spectra of two deposition modes, c-HiPIMS, and a-HiPIMS_B_3. (a) spectral range 285–800 nm, (b) enlargement of the spectral range 425–500 nm.

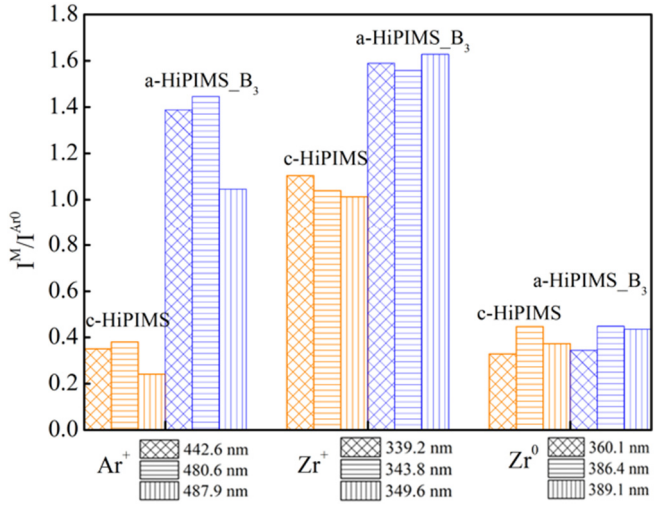

Fig. 4. Evolution of I^M/I^{Ar^0} ratios in the c-HiPIMS mode (in orange) and in the a-HiPIMS_B_3 mode (in blue). (For interpretation of the references to color in this figure legend, the reader is referred to the web version of this article.)

conjunction with the A-type magnetic field distribution summarized in Section 3.1.1.

For the former variation, the mechanism was previously thought to be the converged magnetic lines with the role of a focusing lens on ions, but it contradicts the fact that the ions are not magnetized. Note that the gyration radius of ions (Ar and Zr) in the present deposition system is larger than the characteristic size of the cathode magnetic trap, which causes the ions to be unmagnetized. In this article, we propose that the key to this mechanism is the magnetized electron. During the discharge process, electrons escaping cathode magnetic trap originate from the dense ionization zones (spokes) above the magnetron's racetrack. It has been proved that the electron escaping is driven by the azimuthal electric field inside the spoke (E_θ) with the cathode magnetic field, and its velocity can be obtained via $\boldsymbol{v_e} = \mathbf{E}_\theta \times \mathbf{B}/B^2$ [33]. When electrons enter the region II with $\boldsymbol{v_e}$, there is an angle α between the velocity vector $\boldsymbol{v_e}$ and the magnetic lines. Thus, electrons are bound by the Lorentz force on the magnetic lines and move toward the substrate in a spiral trajectory. Along the magnetic lines, they are then recaptured again in the sub-E × B region.

Now we turn back to the motion of electrons in region II. The motion path of electrons is constrained by the magnetic lines, the velocity v_e of electrons can be numerically estimated by $v_e = E_\theta/B$. At the numerical estimate of v_e, $E_\theta = 10^3$ V/m is taken, which is scaled from studies by A. Anders et al. [33] and N. Brenning et al. [34]. B = 50 mT is taken, which is measured on our magnetron by using the Hall probe positioned by computer-controlled stepper motor. Therefore, $v_e = 2 \times 10^4$ km/s is obtained. It is worth noting that the electron velocity v_e flowing toward the substrate is considerably greater than the ion acoustic speed C_s $(=(kT_e/m_i)^{1/2} \approx 1.9 \times 10^3$ m/s, where k is the Boltzmann constant, T_e is the electron temperature, and m_i is the mass of the Ar ion). This indicates that the modified two-stream instability (MTSI) may be excited, which can accelerate ions in the direction of electron motion [34]. For the ions in the deposition system, they are composed of energetic and thermalized ions [35]. The energetic ions carry sufficient kinetic energy and are therefore less affected by magnetized electrons. Conversely, the motion of the thermalized ions is susceptible to the perturbation potential, since they lose part of energy inside the magnetic trap due to the high probability of collision with the neutral species (gas phase). Therefore, the thermalized ions would be accelerated and focused toward the substrate. Finally, due to the non-magnetization of the ions and the self-bias of the substrate, the ions reaching the vicinity of the substrate would deposit on the substrate without being controlled by the sub-E × B region. As a consequence of this process, it appears that the magnetic lines in Region II eventually concentrate a portion of the ions in front of the substrate. However, the focusing lens character of the A-type magnetic lines actually acts on the electrons. The essence of the focused ions is the excitation of the modified two-stream instability (MTSI) during the electron converging process, which causes the ions to be accelerated and focused in front of the substrate. In addition, it should be mentioned that MTSI may also be excited in the magnetic field of the c-HiPIMS mode. However, the degree of acceleration of ions in c-HiPIMS is much less than that in a-HiPIMS due to (i) the diverging magnetic lines that make the electron loss to the wall of the vacuum chamber and (ii) the smaller value of v_e caused by the stronger magnetic field in the region III of c-HiPIMS.

For the latter variation, the mechanism is the formation of the sub-E × B region. It enhances the collision event between re-capture electrons and neutrals of Ar and Zr, thus increases the ionization rate. In the sub-E × B region, the orthogonal electromagnetic field bends the trajectory of electrons that escape from the cathode and drives the electrons to drift along the **E** × **B** direction, which constrains the electrons in front of the substrate. At the numerical estimation of the E × B drift velocity of the electron, the self-bias potential on the substrate is taken as $U_s = -20$ V, which results from measurements in [36]. The magnetic field value is taken as 10 mT at sub-E × B region due to the rapid decay of the magnetic field strength with distance. Then, the drift

velocity of the electron is $V_{E\times B} \approx 10^5$ m/s. It is comparable to the velocity of electron E × B drift in the cathode magnetic trap [33] and therefore has the potential to excite the impact ionization events. Despite the high ionization rate of HiPIMS, there is still a certain proportion of target atoms. The unionized Zr atoms may further be ionized as they pass through the sub-E × B region. In addition to the effect on the target species, the contribution of the sub-E × B region to Ar atoms has a more pronounced effect. Since the density of Ar atoms is higher than that of Zr atoms, the recaptured electrons have a higher probability to collide with Ar than with Zr atoms. Note that the enhanced ionization of Ar atoms is critical to the formation of the final microstructure of the Zr films because of the atomic peening effect they initiate.

In addition, the parallel magnetic field above the magnetron cathode is slightly broadened and weakened in the a-HiPIMS mode, which facilitates the movement of ionized particles toward the substrate. The deposition of ionized target atoms is strongly blocked by the potential barrier generated by the plasma confinement in the cathode magnetic trap. The “ion return effect” is a significant consequence of this potential barrier. It is known that the height of such a barrier decreases with reducing magnetic field [37]. Therefore, the blocking of the ionized particles is weakened in the a-HiPIMS mode. In addition, the broadened parallel magnetic field is beneficial to the utilization of the target.

Therefore, when the cathode discharge remains unchanged, the application of A-type magnetic field configuration can increase the ion densities (Zr^+ and Ar^+) and enhance the collision events in front of the substrate by generating secondary ionization and weakening the loss of charged particles toward the vacuum wall. As a consequence of more collision events, the bombardment kinetic energy of the plasma will be reduced. It has been proved in [38,39] that the density and kinetic energy of the bombardment plasma are the main factors affecting the final microstructure of the film. In the following, the microstructure and properties of the Zr films are characterized to reveal how the plasma characteristics affect film growth.

3.2. Evolution of the Zr film characteristics

3.2.1. Deposition rate and morphology

The thickness distribution and deposition rate of the Zr film in the c-HiPIMS mode and the a-HiPIMS modes are shown in Fig. 5. The thickness distribution from the center to the edge of the substrate holder (corresponding to the center to the edge of the magnetron) was measured, as shown in Fig. 5(a). It can be seen that the thickness distribution of the film becomes uniform gradually in the a-HiPIMS mode with increasing the magnetic strength. For the films in the c-HiPIMS mode, the maximum thickness is observed in the center of substrate holder where faces the magnetron center. Along the distance away from the center, the thickness of the film gradually decreases. For the films in the a-HiPIMS modes, the film thickness near the center is significantly reduced. Moreover, the closer to the center, the faster the thickness decreases. Instead, the thickness reduction near the edge is small and remains almost unchanged whatever the a-HiPIMS mode considered. Even in the a-HiPIMS_B_3 mode, the thickness distribution from the center to the edge tends to be homogenous. The deposition rate is shown in Fig. 5(b) as a function of the strength of the auxiliary magnetic field from 0 mT to 45 mT, which corresponds to the c-HiPIMS mode and the three a-HiPIMS modes. The deposition rate decreases from 31 to 15 nm min^{-1} with increasing strength of the auxiliary magnetic field. Therefore, it can be stated that as the strength of the auxiliary magnetic field increases, the better thickness homogeneity can be achieved, but at the price of a reduced deposition rate. Since the deposition rate is calculated from the net thickness and the deposition time, the interpretation of the change in deposition rate needs to be combined with the film morphology.

In order to explain the reduced deposition rate, and more importantly, to evaluate the contribution of variations of plasma characteristics to the film morphology during growth, the top surface and cross-sectional SEM micrographs of Zr films in the respective a-HiPIMS modes, as well as in the c-HiPIMS mode are shown in Fig. 6. From the top surface images (left panel), the films deposited in the c-HiPIMS mode exhibit an obvious granular structure and its surface appears rough, while the films deposited in three a-HiPIMS modes show a smoother surface. It can be seen from the cross-sectional images (right panel) that, as the deposition mode evolves from the c-HiPIMS to a-HiPIMS_B_3, the morphology of Zr films becomes denser. The Zr films deposited in c-HiPIMS mode (Fig. 6(e)) exhibits a columnar structure with intercolumnar pores. Instead, the morphology of Zr films deposited in three a-HiPIMS modes (Fig. 6(f)–(h)) appear to be denser, the columns are broken for a-HiPIMS_B_1 (Fig. 6(f)) and tend to disappear with increasing the field strength. In the a-HiPIMS_B_3 mode (Fig. 6 (h)), the columnar structure of the film is even harder to resolve. Therefore, the application of A-type magnetic configuration in the a-HiPIMS modes results in the smoother, denser, and lower porosity Zr films. Such denser morphology of the Zr films is expected to be partially responsible for the decrease in the net deposition rate depicted in Fig. 5. The main cause of the decreased deposition rate is however attributed to the triggering of the resputtering mechanism, which indicated by the top surface morphology of Fig. 6 (d).

The smoother surface and denser morphology are the consequence of variations in characteristics of the bombardment plasma in the sub-E × B region. The action of the A-type magnetic field promotes more collision events, increases the ionization rate of Zr and Ar atoms, as well as appropriately weakens the bombardment kinetic energy of the

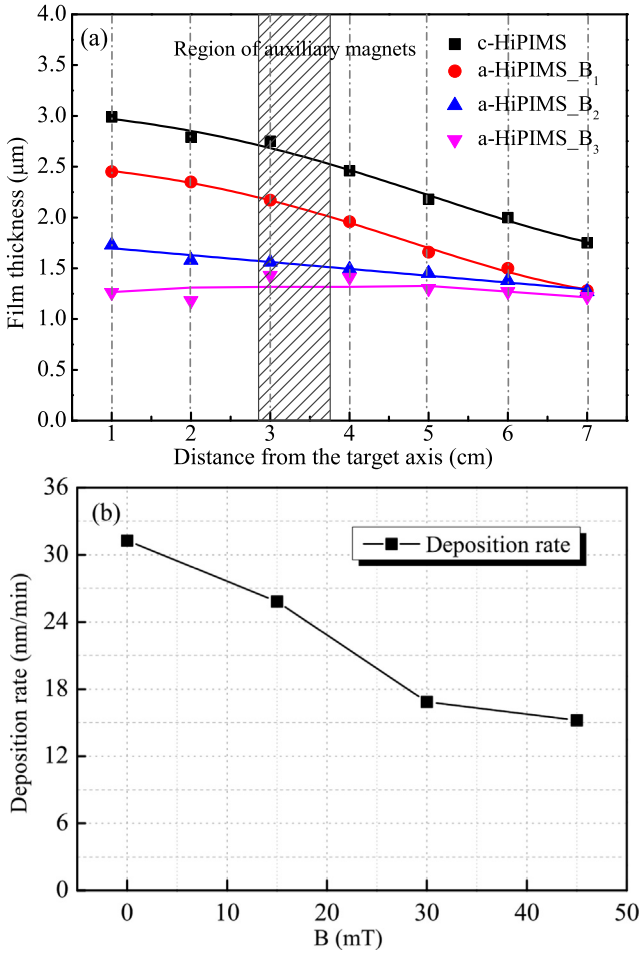

Fig. 5. The thickness distribution (a) and deposition rate (b) as a function of the strength of the auxiliary magnetic field.

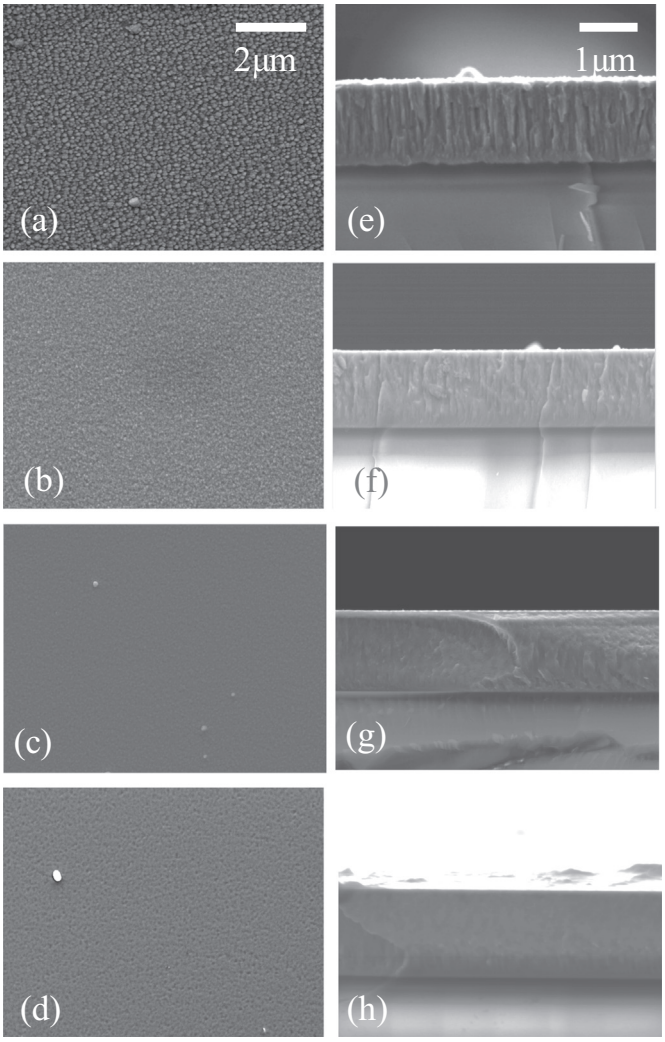

Fig. 6. SEM micrographs of top surface and cross-section of Zr films in: (a, e) c-HiPIMS, (b, f) a-HiPIMS_B_1, (c, g) a-HiPIMS_B_2, and (d, h) a-HiPIMS_B_3.

plasma in front of the substrate. The combination of reduced bombardment energy and increased density are responsible for the smoother surface and denser morphology. The transport trajectory of the plasma with reduced bombardment energy can be effectively twisted by the self-biased electric field which is perpendicular to the substrate surface. The angular distribution (the angle between the incident direction of the plasma and the normal direction of the substrate) of the plasma reaching the substrate thus becomes smaller [35]. Consequently, the plasma with lower angular distribution fills the voids and valleys on the film surface caused by the shadowing effect of ballistic particle transport. The enhanced density of ions would lead to atomic peening effect, which reduces inter- and intra-column porosity and promotes film densification. Previous work [22,40] reported that the disappearance of the columnar structure in the film was due to the enhanced adatom mobility on the film surface, which depends on the bombardment energy of the deposition flux and the substrate temperature. Conversely, the bombardment energy carried by the plasma is not improved in our work. Moreover, the film growth takes place at the condition without external substrate heating, i.e. at a very low homologous temperature (Ts/Tm, where Ts is the substrate temperature and Tm the melting temperature of the coating material). Therefore, the adatom mobility originating from the bombardment energy and the substrate temperature is not improved. It can be concluded that the smoother surface and denser morphology of the Zr films are only contributed by the combination of the high density and the low

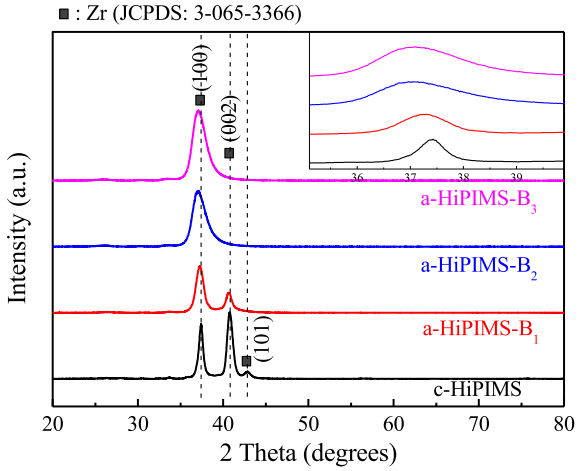

Fig. 7. X-ray diffractograms of the Zr films deposited in different modes on glass substrates.

bombardment energy of the plasma. It is known that the decreased kinetic energy of the film-forming species leads to the film with a rough surface and promotes the creation of porosity because the adatoms have lower surface diffusion ability [40]. However, in our deposition system, this roughening mechanism seems to be well compensated by the high ionization degree.

3.2.2. Structural characteristics of Zr films

Fig. 7 shows the X-ray diffractograms of the Zr films deposited in the c-HiPIMS mode and three a-HiPIMS modes. It can be observed that all Zr films are composed of α-phase with hexagonal structure, and retain crystalline orientations of (100), (002), and (101) without any phases.

One can observe that the diffraction peak (002) is strongly suppressed while the peak (100) is promoted favorably, from c-HiPIMS mode to a-HiPIMS_B_3 mode. That is the transition from randomly oriented to highly (100) oriented crystalline occurs as the strength of auxiliary magnetic field increases. Based on the “survival of the fastest” model [41], the structure of hcp metal films deposited on amorphous substrates are generally expected: crystal nucleation occurs randomly, but polycrystalline films grow along the plane that possesses the lowest surface energy, that is, the initial islands with the densest planes (the largest atom number) are selected. On the contrary, the plane (100) corresponds to the higher surface energy in the hcp structure. The possible explanation for the strong (100) texture (emergence of the high surface energy plane) is that the non-equilibrium deposition process during the film growth provided by the high-density ion bombardment of the sub-E × B region. In the a-HiPIMS modes, although the bombardment kinetic energy of plasma is impaired, the average kinetic energy received per unit area of the substrate may be increased due to the significant increase in plasma density. It results in more kinetic energy being transferred from the deposition plasma into the growing film and thus the preferred orientation (100) peak. The growth of the lattice plane with higher surface energy in the non-equilibrium deposition system is consistent with those reported in [42,43].

The average grain size was determined using the Scherrer's formula from the full width at half maximum (FWHM) of the diffraction peak (100). From the c-HiPIMS mode to the a-HiPIMS_B_3 mode, the average grain size decreases sequentially, being 16.8 nm, 8.6 nm, 6.0 nm, and 5.7 nm, respectively. When the strength of the auxiliary magnetic field exceeds 30mT (the a-HiPIMS_B_2 mode), the grain size remains approximately constant around 6 nm. Generally, grain refinement results in a more dispersed and finer porosity distribution in films, as well as improved mechanical behavior. In recent studies [44,45], grain refinement was achieved by restricting grain growth, in which a common method is to add other elements. For example, a small amount of one of

the metal elements (M1 or M2) in the (M1, M2) alloy is displaced by an added reactive gas (N, O, etc.), that is, a nitride or oxide of (M1, M2) alloy are grown. However, what is required is the grain size of the film can be tailored rather than being just a consequence of alloying. In the present work, the grain refinement is achieved by the high density and the reduced kinetic energy of the bombarding plasma. In the initial stage of film growth, a large amount of the instantaneous Zr ion bombardment produces high initial island density (i.e., more initial nucleation sites) with short diameter. Following, at the growing stage where the islands start to be impinged and coalesce, the driving force for grain refinement springs from three aspects. First, high-density ions arriving at the substrate results in random interruptions of the growing grains and then induces more sites promoting secondary nucleation. Second, the increased bombardment density of Ar ions may displace atoms in the crystal lattice and then lead to point-defects that favor nucleation. Last, the grain refinement is also related to the lower kinetic energy carried by the bombarding ions. When the ions impinge on the substrate surface with the reduced bombardment energy, the local heating is less intense. In this scenario, the reaction of the arriving ions with atoms that already on the film surface is reduced during film growth. It means that the coalescence with nearby atoms on the substrate for forming a larger cluster is more difficult, thus forms smaller sized grains. The last interpretation is equally valid for neutrals in the bombardment plasma. Therefore, altered plasma characteristics limit grain growth. Moreover, it achieves a relative balance in the competition between grain growth and nucleation density, and thus forms a nanocrystal structure with finer grain size. Besides, as a complement to the morphologies observed in SEM (Fig. 6), grain refinement also contributes to the transition of the Zr films from the columnar structure to the denser homogeneous structure one.

The inset of Fig. 7 shows the detailed XRD spectra of the 2theta angle between 35° and 40°. It can be observed that, as the strength of auxiliary magnetic field increases (from c-HiPIMS to a-HiPIMS_B_3), the position of the diffraction peak (100) gradually shifts to a lower angle. This observation indicates the increase of compressive stress and/or reveals lattice expansion. Note that the thermal stress is not considered in the present work because the substrate was not additionally heated during the deposition process. From the inset of Fig. 7, the expanded increment of the lattice parameter *a* is about 0.004 nm. The interplanar spacing d is increased by 0.003 nm. Many studies have been devoted to the relationship between ion bombardment and the residual stress in the film [46–48]. It has been pointed out that the compressive stress is related to defect creation and grain boundaries. For the films in three a-HiPIMS modes, the primary cause of compressive stress residual in the film is the refinement of grain size. This is consistent with the studies of [47–49]. The grain refinement promotes the high density of grain boundaries, which consequently results in compressive stress. Meanwhile, the condition of bombardment plasma in the a-HiPIMS modes suppresses the defect annihilation which is the weakening mechanism of compressive stress. The reduced kinetic energy is insufficient to produce a local self-heating corresponding to local defect annealing (stress relaxation) [46,50,51].

3.2.3. Mechanical properties

The mechanical properties of Zr films, hardness H and effective Young's modulus E^*, are presented in Fig. 8(a). They are the average values of ten measurements performed on each sample since two extremum values (maximum and minimum) in the measurement data were removed. To eliminate the effect of viscoelasticity, the loading and unloading processes were separated by 5 s holding time. With increasing the magnetic strength of auxiliary magnetic field (from c-HiPIMS to a-HIPIMS_B_3) the hardness rises from 5.7 GPa to 16.8 GPa. Simultaneously, the effective Young's modulus is slightly reduced from 140 to 131 GPa.

Factors affecting film hardness include grain size, residual stress and preferred orientation. Here, the most significant factor for the increased

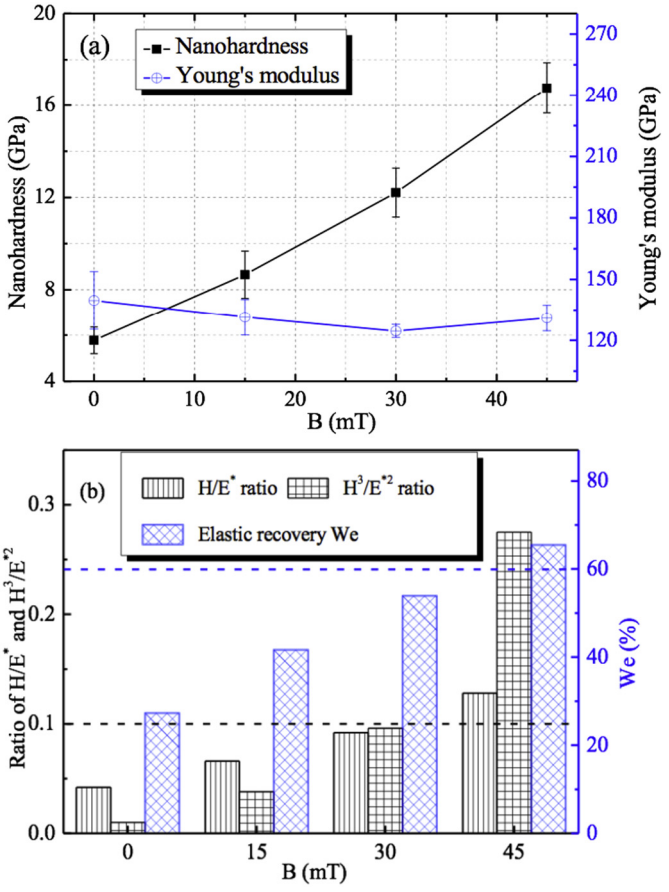

Fig. 8. (a) Hardness and effective Young's modulus and (b) ratios H/E^*, H^3/E^{*2} and elastic recovery W_e as a function of the strength of the auxiliary magnetic field.

hardness in the a-HiPIMS modes is assumed to be the grain refinement. The main trend of increased hardness is consistent with the well-known Hall–Petch [52] relation "$H = H_0 + K_H d^{-1/2}$". However, from a-HIPIMS_B_1 to a-HIPIMS_B_3 segment, the hardness maintains an approximately linear increase, while the rate of refinement of the grain size is slow (from 16.8 nm, 8.6 nm, 6.0 nm, to 5.7 nm). Inconsistent with the prediction of the Hall-Petch relation, during this period, the hardness increment is not sufficient to be provided by the proportion of sole grain refinement. It suggests that the increased hardness from a-

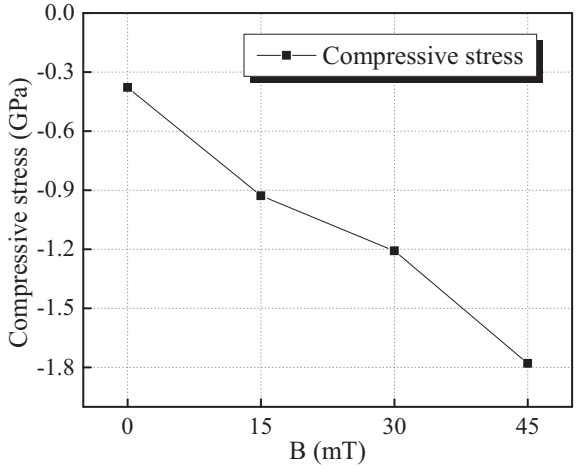

Fig. 9. The compressive stress σ as a function of the strength of the auxiliary magnetic field.

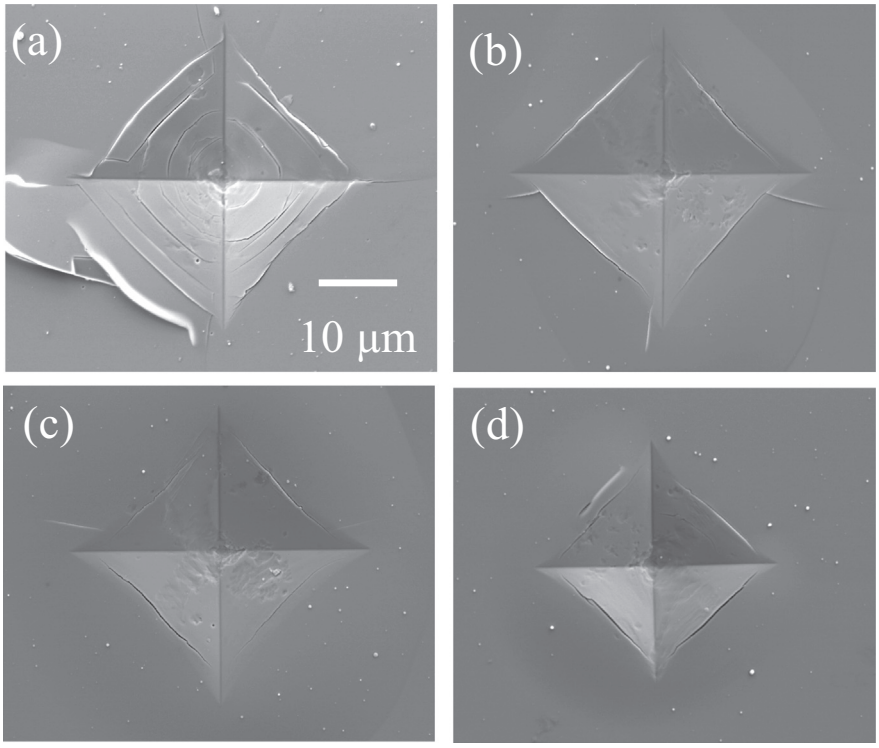

Fig. 10. Morphology of the Vickers indentations on the film surface deposited under different modes: (a) c-HiPIMS (b) a-HiPIMS_B_1, (c) a-HiPIMS_B_2 and (d) a-HiPIMS_B_3, with load L = 20 N.

HIPIMS_B_1 to a-HIPIMS_B_3 segment may also result from the compressive stress [22,53]. Fig. 9 illustrates the compressive stress σ in the films as a function of the strength of the auxiliary magnetic field. The large increase in σ from a-HIPIMS_B_1 to a-HIPIMS_B_3 segment coincides with the hardness increase in this segment.

The slightly reduced effective Young's modulus E^* is independent of the effect of grain size but depends on the preferred orientation. Young's modulus is anisotropic and is related to the atomic coordination and electron redistribution (bond saturation) on the crystal plane [54,55]. As presented in Fig. 7, the diffraction peaks (100), (002) and (101) coexist under the films of the c-HIPIMS mode. With the application of the A-type magnetic field, (100) is promoted while (002) is suppressed, and the (100) peak becomes dominant finally. The decrease in the effective Young's modulus E^* of the Zr film having this preferred orientation can be explained by the E^* of the Zr (100) plane that is less than the E^* of the (002) plane. This dependence between effective Young's modulus and preferred orientation is similar to that in the literature [55,56].

The mechanical behavior of films is also characterized by the ratio H/E^*, the ratio H^3/E^{*2} and the elastic recovery W_e. The failure of the elastic strain of film depends on the ratio H/E^* that characterizes the resistance of the material to elastic deformation, while the material's ability to dissipate energy during plastic deformation is characterized by the ratio H^3/E^{*2} [57,58]. It has been shown that the a-HiPIMS mode strongly influences the morphology, microstructure and phase composition of the film, resulting in a substantial increase in hardness H and a slight decrease in effective Young's modulus E^*. Such changes in the film properties are desirable since it indicates better toughness and resistance of the material against plastic deformation (i.e., higher values of H/E^* and H^3/E^{*2}), which are important parameters for determining whether a film is suitable for practical applications [57]. The values of H/E^*, H^3/E^{*2} and W_e of the film are shown in Fig. 8(b), which increases with the strength of the auxiliary magnetic field. For the strong auxiliary magnetic field, a-HiPIMS_B_3 mode, $H/E^* > 0.1$, $H^3/E^{*2} \approx 0.275$, and $W_e > 60\%$. This result indicates that the a-HiPIMS_B_3 deposition mode appears to be a good solution for the preparation of Zr films with improved toughness, since the high values of H^3/E^{*2} and W_e allow the applied high load to be distributed over a wider contact area. This expected performance needs to be confirmed by the morphology of the indentations under high load. The results of the high load test are given in Fig. 10.

Fig. 10 displays the SEM micrographs of Vickers indentations at high load L = 20 N on the surface of the Zr films under different deposition modes. From c-HiPIMS mode to a-HiPIMS_B_3 mode, the radial and circumferential cracks gradually decrease. The film in the a-HiPiMS_B_3 mode (Fig. 9(d)) is found to have the least visible radial cracks and minimal indentation size. It confirms the improved film toughness is obtained in the a-HiPIMS_B_3 mode. The improved toughness is explained as grain refinement and defect accumulation in the deposited Zr film induced by the high-density bombardment effect under the a-HiPIMS modes, which leads to the strengthening of the film toughness [59]. In addition, the improved toughness of the film is also related to the compressive stress (shown in Fig. 9) that makes the crack close and terminates its propagation [60].

4. Conclusion

This article proposes an A-type magnetic field configuration in HiPIMS for effectively controlling plasma behavior near the substrate and expanding the range of HiPIMS applications. Due to the sub-E × B region and converging magnetic lines toward the substrate induced by the A-type magnetic field configuration, a large number of magnetized electrons can be recaptured and re-energized in front of the substrate. The bombardment density of the plasma near the substrate can thus be enhanced while the cathode discharge parameters are kept constant.

The evolution of microstructure and mechanical properties of Zr films prepared by conventional HiPIMS mode (c-HiPIMS) and A-type magnetic field HiPIMS mode (a-HiPIMS_B_1/B_2/B_3) were investigated. When the deposition mode transitions from c-HiPIMS to a-HiPIMS_B_3, the Zr film has a smoother surface and a denser cross-sectional

morphology, finer grains (from 16.8 nm to 5.5 nm), strong (100) texture, and more homogenous thickness distribution. The hardness increases from 6 GPa to 17 GPa, while the effective Young's modulus decreases slightly from 140 to 131 GPa. Moreover, the ratio $H/E^* > 0.1$ and the elastic recovery $W_e > 60\%$ at the a-HiPIMS_B_3 deposition mode.

It is demonstrated that the plasma characteristics altered by the proposed A-type magnetic field configuration can balance the competition between grain growth and nucleation density, thereby obtaining grain refinement, densification, and thus higher mechanical properties in the Zr films without high energy ion bombardment. It compensates for a shortcoming of substrate bias, i.e., the ineffectiveness of "bias-promoting dense film" on the electrically insulating substrates. In addition, this A-type magnetic field configuration reinforces the benefit of conventional HiPIMS technology as a means of achieving high ion fraction plasma assisted deposition. We believe that the proposed A-type magnetic configuration can also be applied to the preparation of thin films composed of other elements or alloys to improve their microstructure and mechanical properties.

Author contributions

Huan LUO took part in the HiPIMS experiment, magnetic field simulation, samples characterization, and paper writing. Fei GAO took part in the discussion of results, paper revising. Alain BILLARD participated in the HiPIMS experiment and samples characterization and was primarily responsible for the revision of the paper. All authors contributed to the writing and editing of the manuscript. All authors discussed the text and commented on the manuscript.

Declaration of Competing Interest

None.

Acknowledgments

The authors thank the China Scholarship Council (No. 201604490110) and Pays de Montbéliard Agglomeration for their financial support of this study.

References

[1] H.O. Pierson, Handbook of Refractory Carbides and Nitrides, Noyes Publications, New Jersey, USA, 1996, pp. 181–205.
[2] E.S. Fisher, C.J. Renken, Single-crystal elastic moduli and the hcp → bcc transformation in Ti, Zr, and Hf, Phys. Rev. 135 (1964) A482, https://doi.org/10.1103/PhysRev.135.A482.
[3] L.E. Toth, Transition Metal and Carbides, Academic Press, New York, 1971.
[4] P. Ashcheulov, R. Skoda, J. Skarohlid, A. Taylor, F. Fendrych, I. Kratochvílová, Layer protecting the surface of zirconium used in nuclear reactors, Recent. Pat. Nanotech. 10 (2016) 59–65.
[5] K.J. Hollis, M.E. Hawley, P.O. Dickerson, Characterization of thermal diffusion related properties in plasma sprayed zirconium coatings, J. Therm. Spray Techn. 21 (2012) 409–415, https://doi.org/10.1007/s11666-011-9718-x.
[6] K.J. Hollis, Zirconium diffusion barrier coatings for uranium fuel used in nuclear reactors, Adv. Mater. Process. 168 (2010) 57–59.
[7] R.K. Bamola, Thermal Sprayed Zirconium Coatings for Corrosion Resistance, PhD Thesis SUNY, Stony Brook, 1992 May.
[8] Y.C. Kang, M.M. Milovancev, D.A. Clauss, M.A. Lange, R.D. Ramsier, Ultra-high vacuum investigation of the surface chemistry of zirconium, J. Nucl. Mater. 281 (2000) 57–64, https://doi.org/10.1016/S0022-3115(00)00131-8.
[9] A. Singh, P. Kuppusami, R. Thirumurugesan, R. Ramaseshan, M. Kamruddin, S. Dash, V. Ganesan, E. Mohandas, Study of microstructure and nanomechanical properties of Zr films prepared by pulsed magnetron sputtering, Appl. Surf. Sci. 257 (2011) 9909–9914, https://doi.org/10.1016/j.apsusc.2011.06.106.
[10] J. Chakraborty, K.K. Kumar, S. Mukherjee, S.K. Ray, Stress, texture and microstructure of zirconium thin films probed by X-ray diffraction, Thin Solid Films 516 (2008) 8479–8486, https://doi.org/10.1016/j.tsf.2008.04.096.
[11] L. Pichon, T. Girardeau, F. Lignou, A. Straboni, Evidence of ω-phase in ion beam sputtered zirconium thin films, Thin Solid Films 342 (1999) 93–99, https://doi.org/10.1016/S0040-6090(98)01425-4.
[12] D. Pilloud, J.F. Pierson, C. Rousselot, F. Palmino, Substrate effect on the formation of ω-phase in sputtered zirconium films, Scr. Mater. 53 (2005) 1031–1036, https://doi.org/10.1016/j.scriptamat.2005.07.011.
[13] J.T. Gudmundsson, N. Brenning, D. Lundin, U. Helmersson, High power impulse magnetron sputtering discharge, J. Vac. Sci. Technol. A 30 (2012) 030801, , https://doi.org/10.1116/1.3691832.
[14] M. Samuelsson, D. Lundin, J. Jensen, M.A. Raadu, J.T. Gudmundsson, U. Helmersson, On the film density using high power impulse magnetron sputtering, Surf. Coat. Technol. 205 (2010) 591–596, https://doi.org/10.1016/j.surfcoat.2010.07.041.
[15] J.W. Lim, J.W. Bae, Y.F. Zhu, S. Lee, K. Mimura, M. Isshiki, Improvement of Zr film purity by using a purified sputtering target and negative substrate bias voltage, Surf. Coat. Technol. 201 (2006) 1899–1901, https://doi.org/10.1016/j.surfcoat.2006.01.009.
[16] M. Samuelsson, J. Jensen, U. Helmersson, L. Hultman, H. Högberg, ZrB2 thin films grown by high power impulse magnetron sputtering from a compound target, Thin Solid Films 526 (2012) 163–167, https://doi.org/10.1016/j.tsf.2012.11.006.
[17] M. Lv, X. Xiu, Z. Pang, Y. Dai, S. Han, Influence of the deposition pressure on the properties of transparent conducting zirconium-doped zinc oxide films prepared by RF magnetron sputtering, Appl. Surf. Sci. 252 (2006) 5687–5692, https://doi.org/10.1016/j.apsusc.2005.07.042.
[18] J.M. Urreaga, M.C. Matıas, V. Lorenzo, M.U. De la Orden, Abrasion resistance in the Tumble test of sol–gel hybrid coatings for ophthalmic plastic lenses, Mater. Lett. 45 (2000) 293–297, https://doi.org/10.1016/S0167-577X(00)00120-8.
[19] H. Chatham, Oxygen diffusion barrier properties of transparent oxide coatings on polymeric substrates, Surf. Coat. Technol. 78 (1996) 1–9, https://doi.org/10.1016/0257-8972(95)02420-4.
[20] M. Tanahashi, T. Yao, T. Kokubo, M. Minoda, T. Miyamoto, T. Nakamura, T. Yamamuro, Apatite coating on organic polymers by a biomimetic process, J. Am. Ceram. Soc. 77 (1994) 2805–2808, https://doi.org/10.1111/j.1151-2916.1994.tb04508.x.
[21] S. Tsikata, T. Minea, Modulated electron cyclotron drift instability in a high-power pulsed magnetron discharge, Phys. Rev. Lett. 114 (2015) 185001, , https://doi.org/10.1103/PhysRevLett.114.185001.
[22] I.L. Velicu, V. Tiron, C. Porosnicu, I. Burducea, N. Lupu, G. Stoian, G. Popa, D. Munteanu, Enhanced properties of tungsten thin films deposited with a novel HiPIMS approach, Appl. Surf. Sci. 424 (2017) 397–406, https://doi.org/10.1016/j.apsusc.2017.01.067.
[23] R. Ganesan, B. Akhavan, X. Dong, D.R. McKenzie, M.M.M. Bilek, External magnetic field increases both plasma generation and deposition rate in HiPIMS, Surf. Coat. Technol. 352 (2018) 671–679, https://doi.org/10.1016/j.surfcoat.2018.02.076.
[24] J. Wu, B.H. Wu, D.L. Ma, D. Xie, Y.P. Wu, C.Z. Chen, Y.T. Li, H. Sun, N. Huang, Y.X. Leng, Effects of magnetic field strength and deposition pressure on the properties of TiN films produced by high power pulsed magnetron sputtering (HPPMS), Surf. Coat. Technol. 315 (2017) 258–267, https://doi.org/10.1016/j.surfcoat.2017.02.051.
[25] V. Tiron, I.L. Velicu, I. Mihăilă, G. Popa, Deposition rate enhancement in HiPIMS through the control of magnetic field and pulse configuration, Surf. Coat. Technol. 337 (2018) 484–491, https://doi.org/10.1016/j.surfcoat.2018.01.065.
[26] J. Alami, V. Stranak, A.P. Herrendorf, Z. Hubicka, R. Hippler, Design of magnetic field configuration for controlled discharge properties in highly ionized plasma, Plasma Sources Sci. Technol. 24 (2015) 045016, , https://doi.org/10.1088/0963-0252/24/4/045016.
[27] D. Lundin, U. Helmersson, S. Kirkpatrick, S. Rohde, N. Brenning, Anomalous electron transport in high power impulse magnetron sputtering, Plasma Sources Sci. Technol. 17 (2008) 025007, , https://doi.org/10.1088/0963-0252/17/2/025007.
[28] A. Hecimovic, Anomalous cross-B field transport and spokes in HiPIMS plasma, J. Phys. D. Appl. Phys. 49 (2016) 18LT01, https://doi.org/10.1088/0022-3727/49/18/18LT01.
[29] D. Lundin, P. Larsson, E. Wallin, M. Lattemann, N. Brenning, U. Helmersson, Cross-field ion transport during high power impulse magnetron sputtering, Plasma Sources Sci. Technol. 17 (2008) 035021, , https://doi.org/10.1088/0963-0252/17/3/035021.
[30] W.C. Oliver, G.M. Pharr, An improved technique for determining hardness and elastic modulus using load and displacement sensing indentation experiments, J. Mater. Res. 7 (1992) 1564–1583, https://doi.org/10.1557/JMR.1992.1564.
[31] B.K. Gan, M.M.M. Bilek, D.R. McKenzie, M.B. Taylor, D.G. McCulloch, Effect of intrinsic stress on preferred orientation in AlN thin films, J. Appl. Phys. 95 (2004) 2130–2134, https://doi.org/10.1063/1.1640462.
[32] I. Ivanov, P. Kazansky, L. Hultman, I. Petrov, J.E. Sundgren, Influence of an external axial magnetic field on the plasma characteristics and deposition conditions during direct current planar magnetron sputtering, J. Vac. Sci. Technol. A 12 (1994) 314–320, https://doi.org/10.1116/1.578874.
[33] A. Anders, P. Ni, A. Rauch, Drifting localization of ionization runaway: unraveling the nature of anomalous transport in high power impulse magnetron sputtering, J. Appl. Phys. 111 (2012) 053304, , https://doi.org/10.1063/1.3692978.
[34] N. Brenning, D. Lundin, T. Minea, C. Costin, C. Vitelaru, Spokes and charged particle transport in HiPIMS magnetrons, J. Phys. D-Appl. Phys. 46 (2013) 084005, , https://doi.org/10.1088/0022-3727/46/8/084005.
[35] J.C. Oliveira, F. Ferreira, A. Anders, A. Cavaleiro, Reduced atomic shadowing in HiPIMS: role of the thermalized metal ions, Appl. Surf. Sci. 433 (2018) 934–944, https://doi.org/10.1016/j.apsusc.2017.10.133.
[36] M. Balzer, M. Fenker, Three-dimensional thickness and property distribution of TiC films deposited by DC magnetron sputtering and HIPIMS, Surf. Coat. Technol. 250 (2014) 37–43, https://doi.org/10.1016/j.surfcoat.2014.02.011.
[37] J.W. Bradley, A. Mishra, P.J. Kelly, The effect of changing the magnetic field strength on HiPIMS deposition rates, J. Phys. D. Appl. Phys. 48 (2015) 215202, , https://doi.org/10.1088/0022-3727/48/21/215202.

[38] J.Z. Lu, L.J. Wu, G.F. Sun, K.Y. Luo, Y.K. Zhang, J. Cai, C.Y. Cui, X.M. Luo, Microstructural response and grain refinement mechanism of commercially pure titanium subjected to multiple laser shock peening impacts, Acta Mater. 127 (2017) 252–266, https://doi.org/10.1016/j.actamat.2017.01.050.
[39] F. Cemin, G. Abadias, T. Minea, C. Furgeaud, F. Brisset, D. Solas, D. Lundin, Benefits of energetic ion bombardment for tailoring stress and microstructural evolution during growth of Cu thin films, Acta Mater. 141 (2017) 120–130, https://doi.org/10.1016/j.actamat.2017.09.007.
[40] Z. Wang, D. Zhang, P. Ke, X. Liu, A. Wang, Influence of substrate negative bias on structure and properties of TiN coatings prepared by hybrid HIPIMS method, J. Mater. Sci. Technol. 31 (2015) 37–42, https://doi.org/10.1016/j.jmst.2014.06.002.
[41] A. Van der Drift, Evolutionary selection, a principle governing growth orientation in vapour-deposited layers, Philips Res. Rep. 22 (1967) 267.
[42] D.M. Devia, E. Restrepo-Parra, P.J. Arango, A.P. Tschiptschin, J.M. Velez, TiAlN coatings deposited by triode magnetron sputtering varying the bias voltage, Appl. Surf. Sci. 257 (2011) 6181–6185, https://doi.org/10.1016/j.apsusc.2011.02.027.
[43] Q. Ma, L. Li, Y. Xu, J. Gu, L. Wang, Y. Xu, Effect of bias voltage on TiAlSiN nanocomposite coatings deposited by HiPIMS, Appl. Surf. Sci. 392 (2017) 826–833, https://doi.org/10.1016/j.apsusc.2016.09.028.
[44] M.A. Easton, D.H. StJohn, A. Prasad, Grain refinement of aluminium alloys: Recent developments in predicting the as-cast grain size of alloys refined by Al-Ti-B master alloys, Light Metals, Springer, Cham, 2014, pp. 939–944, , https://doi.org/10.1007/978-3-319-48144-9_156.
[45] S. Imura, T. Watabe, K. Miyakawa, K. Hagiwara, H. Ohtake, M. Kubota, Effects of grain refinement on surface enhancement of thin-film chlorine-doped crystalline selenium, J. Mater. Sci.-Mater. el. 28 (2017) 7064–7069, https://doi.org/10.1007/s10854-016-6311-6.
[46] A. Debelle, G. Abadias, A. Michel, C. Jaouen, Stress field in sputtered thin films: ion irradiation as a tool to induce relaxation and investigate the origin of growth stress, Appl. Phys. Lett. 84 (2004) 5034–5036, https://doi.org/10.1063/1.1763637.
[47] E. Chason, B.W. Sheldon, L.B. Freund, J.A. Floro, S.J. Hearne, Origin of compressive residual stress in polycrystalline thin films, Phys. Rev. Lett. 88 (2002) 156103, , https://doi.org/10.1103/PhysRevLett.88.156103.
[48] D. Magnfält, G. Abadias, K. Sarakinos, Atom insertion into grain boundaries and stress generation in physically vapor deposited films, Appl. Phys. Lett. 103 (2013) 051910, , https://doi.org/10.1063/1.4817669.
[49] D. Magnfält, A. Fillon, R.D. Boyd, U. Helmersson, K. Sarakinos, G. Abadias, Compressive intrinsic stress originates in the grain boundaries of dense refractory polycrystalline thin films, J. Appl. Phys. 119 (2016) 055305, , https://doi.org/10.1063/1.4941271.
[50] C.A. Davis, A simple model for the formation of compressive stress in thin films by ion bombardment, Thin Solid Films 226 (1993) 30–34, https://doi.org/10.1016/0040-6090(93)90201-Y.
[51] M.M.M. Bilek, D.R. McKenzie, A comprehensive model of stress generation and relief processes in thin films deposited with energetic ions, Surf. Coat. Technol. 200 (2006) 4345–4354, https://doi.org/10.1016/j.surfcoat.2005.02.161.
[52] M. Zhao, J.C. Li, Q. Jiang, Hall–Petch relationship in nanometer size range, J. Alloy. Compd. 361 (2003) 160–164, https://doi.org/10.1016/S0925-8388(03)00415-8.
[53] M. Bai, K. Kato, N. Umehara, Y. Miyake, Nanoindentation and FEM study of the effect of internal stress on micro/nano mechanical property of thin CNx films, Thin Solid Films 377 (2000) 138–147, https://doi.org/10.1016/S0040-6090(00)01314-6.
[54] T.D. Shen, C.C. Koch, T.Y. Tsui, G.M. Pharr, On the elastic moduli of nanocrystalline Fe, Cu, Ni, and Cu–Ni alloys prepared by mechanical milling/alloying, J. Mater. Res. 10 (1995) 2892–2896, https://doi.org/10.1557/JMR.1995.2892.
[55] L.G. Zhou, H. Huang, Are surfaces elastically softer or stiffer? Appl. Phys. Lett. 84 (2004) 1940–1942, https://doi.org/10.1063/1.1682698.
[56] C.S. Chen, C.P. Liu, C.Y. Tsao, Influence of growth temperature on microstructure and mechanical properties of nanocrystalline zirconium carbide films, Thin Solid Films 479 (2005) 130–136, https://doi.org/10.1016/j.tsf.2004.11.196.
[57] A. Leyland, A. Matthews, On the significance of the H/E ratio in wear control: a nanocomposite coating approach to optimised tribological behavior, Wear 246 (2000) 1–11, https://doi.org/10.1016/S0043-1648(00)00488-9.
[58] J. Blažek, J. Musil, P. Stupka, R. Čerstvý, J. Houška, Properties of nanocrystalline Al–Cu–O films reactively sputtered by DC pulse dual magnetron, Appl. Surf. Sci. 258 (2011) 1762–1767, https://doi.org/10.1016/j.apsusc.2011.10.039.
[59] X. Xie, C. Chen, Y. Xie, Z. Ren, E. Aubry, G. Ji, H. Liao, A novel approach for fabricating Ni-coated FeSiAl soft magnetic composite via cold spraying, J. Alloy. Compd. 749 (2018) 523–533, https://doi.org/10.1016/j.jallcom.2018.03.306.
[60] J. Musil, M. Louda, Z. Soukup, Relationship between mechanical properties and coefficient of friction of sputtered a-C/Cu composite thin films, Diam. Relat. Mater. 17 (2008) 1905–1911, https://doi.org/10.1016/j.diamond.2008.04.009.